A novel QA phantom based on scintillating fiber ribbons with implementation of 2D dose tomography for small-field radiotherapy

Josué Esteves, Odran Pivot, Julien Ribouton, Patrice Jalade, Abdelaali Zouaoui, Laurent Desbat, Simon Rit, Frédéric Blanc, Guido Haefeli, Plamen Hopchev, et al.

Received: 8 March 2022 | Revised: 10 July 2022 | Accepted: 20 July 2022

DOI: 10.1002/mp.15902

RESEARCH ARTICLE

MEDICAL PHYSICS

A novel QA phantom based on scintillating fiber ribbons with implementation of 2D dose tomography for small-field radiotherapy

Josué Esteves[1] | **Odran Pivot**[2] | **Julien Ribouton**[3] | **Patrice Jalade**[3] | **Abdelaali Zouaoui**[1] | **Laurent Desbat**[2] | **Simon Rit**[4] | **Frédéric Blanc**[5] | **Guido Haefeli**[5] | **Plamen Hopchev**[5] | **Jean-Marc Galvan**[1] | **Guo-Neng Lu**[1] | **Patrick Pittet**[1]

[1]Univ Lyon, Université Claude Bernard Lyon 1, CNRS, INSA Lyon, Ecole Centrale de Lyon, CPE Lyon, INL, UMR5270, Villeurbanne, France

[2]Univ. Grenoble Alpes, CNRS, Grenoble INP, TIMC, Grenoble, France

[3]Service de Radiophysique et Radiovigilance, Centre Hospitalier Lyon Sud, Hospices Civils de Lyon, Pierre-Bénite, France

[4]Univ Lyon, INSA-Lyon, Université Claude Bernard Lyon 1, UJM-Saint Etienne, CNRS, Inserm, CREATIS UMR 5220, U1294, CREATIS, Lyon, France

[5]LPHE EPFL, Lausanne, Switzerland

Correspondence
Patrick Pittet, INL-UMR5270, bâtiment Iréne Joliot Curie, Université Claude Bernard Lyon 1, 43 boulevard du 11 novembre 1918, Villeurbanne F-69622, France.
Email: patrick.pittet@univ-lyon1.fr

Funding information
ITMO Cancer AVIESAN, Grant/Award Number: 18CP125-00; LABEX PRIMES, Grant/Award Number: ANR-11-LABX-0063; Investissements d'Avenir, Grant/Award Number: ANR-11-IDEX-0007; Swiss National Science Foundation, Grant/Award Number: 166208

Abstract

Purpose: To develop a novel instrument for real-time quality assurance (QA) procedures in radiotherapy. The system implements a scintillation-based phantom and associated signal acquisition and processing modules and aims to monitor two-dimensional (2D) dose distributions of small fields.

Materials and methods: For the proposed phantom, we have designed and realized a prototype implementing six high-resolution tissue-equivalent scintillating fiber ribbons stacked with in-plane 30° rotated orientations from each other. Each ribbon output is coupled to a silicon photodiode linear array (with an element pitch of 400 μm) to detect scintillating signal, which represents the projected irradiation profile perpendicular to the ribbon's orientation. For the system providing six acquired projected dose profiles at different orientations, we have developed a two-step signal processing method to perform 2D dose reconstruction. The first step is to determine irradiation field geometry parameters using a tomographic geometry approach, and the second one is to perform specific penumbra estimation. The QA system prototype has been tested on a Novalis TrueBeam STX with a 6-MV photon beam for small elliptic fields defined by 5- and 10-mm cone collimators and for 10 × 10- and 20 × 10-mm^2 rectangular fields defined by the micro-multileaf collimator. Gamma index analysis using EBT3 films as reference has been carried out with tight 2%-dose-difference (DD)/700-μm-distance-to-agreement (DTA) as well as 1%-DD/1-mm-DTA criteria for evaluating the system performances. The testing also includes an evaluation of the proposed two-step field reconstruction method in comparison with two conventional methods: filtered back projection (FBP) and simultaneous iterative reconstruction technique (SIRT).

Results: The reconstructed 2D dose distributions have gamma index pass rates higher than 95% for all the tested configurations as compared with EBT3 film measurements with both 2%-DD/700-μm-DTA and 1%-DD/1-mm criteria. 2D global gamma analysis shows that the two-step and FBP radiation field reconstruction methods systematically outperform the SIRT approach. Moreover, higher gamma index success rates are obtained with the two-step method than with FBP in the case of the fields defined with the stereotactic cones.

Conclusions: The proposed small-field QA system makes a use of six water-equivalent scintillating detectors (fiber ribbons) to acquire dose distribution. The developed two-step signal processing method performs tomographic 2D dose reconstruction. A system prototype has been built and tested using hospital facilities with small rectangular and elliptic fields. Testing results show 2D reconstructed dose distributions with high accuracy and resolution. Such a system could potentially be an alternative approach to film dosimetry for small-field QA, which is still widely used as reference in clinical practice.

KEYWORDS
2D dose tomography, small-field dosimetry, water-equivalent scintillating detectors

1 | INTRODUCTION

Recent developments in megavoltage photon-beam radiotherapy mark increasing interest in delivery of highly conformal dose distributions. They are associated with an escalation in the use of small radiation fields, which requires accurate dosimetry, paramount for safety, and efficient use of radiation.[1] This has led to suggestions of measurements of field output factors and lateral beam profiles included in commissioning and periodic quality assurance (QA) procedures.[2]

However, there are challenging issues when implementing small-field dosimetry and QA.[3] In particular, absorbed dose distributions are characterized by (i) a lack of charged particle equilibrium over most of the radiation field, (ii) partial source occlusion by the collimation system of the LINAC, and (iii) important contribution of penumbrae where dose variations show steep gradients.[2] Penumbra is a region of dose falloff around the geometric beam edge due (i) to the transmission through the collimator jaws (transmission penumbra), (ii) to finite source size (geometric penumbra), and (iii) to in-patient X ray scatter (scatter penumbra).[4] It is also noted that there are fewer low-energy photons scattered from LINAC head and phantom and reaching the field center in the case of small field.[5] This results in a hardening of photon energy spectrum (i.e., an increase in average photon energy) at any point on the beam axis.[2]

For the choice or design of detectors for small-field QA, there are small-field issues with significant penumbrae contribution to be considered: volume averaging effect, field size dependence of response related to energy dependence, absorbed dose rate dependence, water equivalence, and dose perturbation.[2,3,6]

IPEM Report 103 has suggested some commercially available detectors to resolve the penumbra in small photon fields: tissue-equivalent radiochromic film, diodes (stereotactic, shielded or unshielded and oriented parallel to central axis), diamond detectors, small air filled ionization chambers, and liquid ionization chambers.[7] A review of detectors by Das et al.[1] has also pointed out that smaller volume devices with water equivalence are best suited for small-field applications. In-line with these recommendations, a protocol for output factor measurements has been proposed by the French Institute for Radiological Protection and Nuclear Safety (IRSN), with a combined use of radiochromic films and micro-chips thermoluminescent dosimeters.[7]

This protocol has now been widely adopted for commissioning procedures. However, it cannot be considered for daily QA as the readout procedure is very time-consuming and the use of disposable films would rapidly increase running costs. Moreover, EBT3 films require a careful control of film processing and read-out procedures for accurate dosimetry.[8] On the other hand, solid-state detectors such as diodes and microdiamonds have also been studied for small-field dosimetry.[9–11] With silicon diode arrays, which are not water equivalent, a sufficient spacing should be respected to avoid any fluence perturbation issue. This necessary condition limits the achievable spatial resolution for small-field QA.

These studies show the advantage of microdiamonds in terms of lower energy dependence compared to silicon diodes, but they also present the drawback of a larger size (2.2-mm detector diameter), which is not suitable for QA of the smallest fields.[12] It has been recently suggested to use an inorganic scintillating point detector to scan the field with submillimeter resolutions.[13,14] However, point (i.e., small volume) detectors could introduce additional uncertainty due to placement errors in high-dose gradient regions. One suggestion to tackle this issue was to implement point detectors in array form.[15]

In this paper, we present the development of a QA phantom, by using six arrays of detectors instead of a single one. The system has been designed to implement tomographic dosimetry for small-field QA. It has been tested using small static rectangular and elliptic fields defined by multileaf collimator (MLC) and stereotactic cones in 6-MV photon beams. Three field reconstruction methods have been tested: a two-step reconstruction method specifically developed for radiation field reconstruction and two other reference methods, filtered back projection (FBP) and simultaneous iterative reconstruction technique (SIRT).[16]

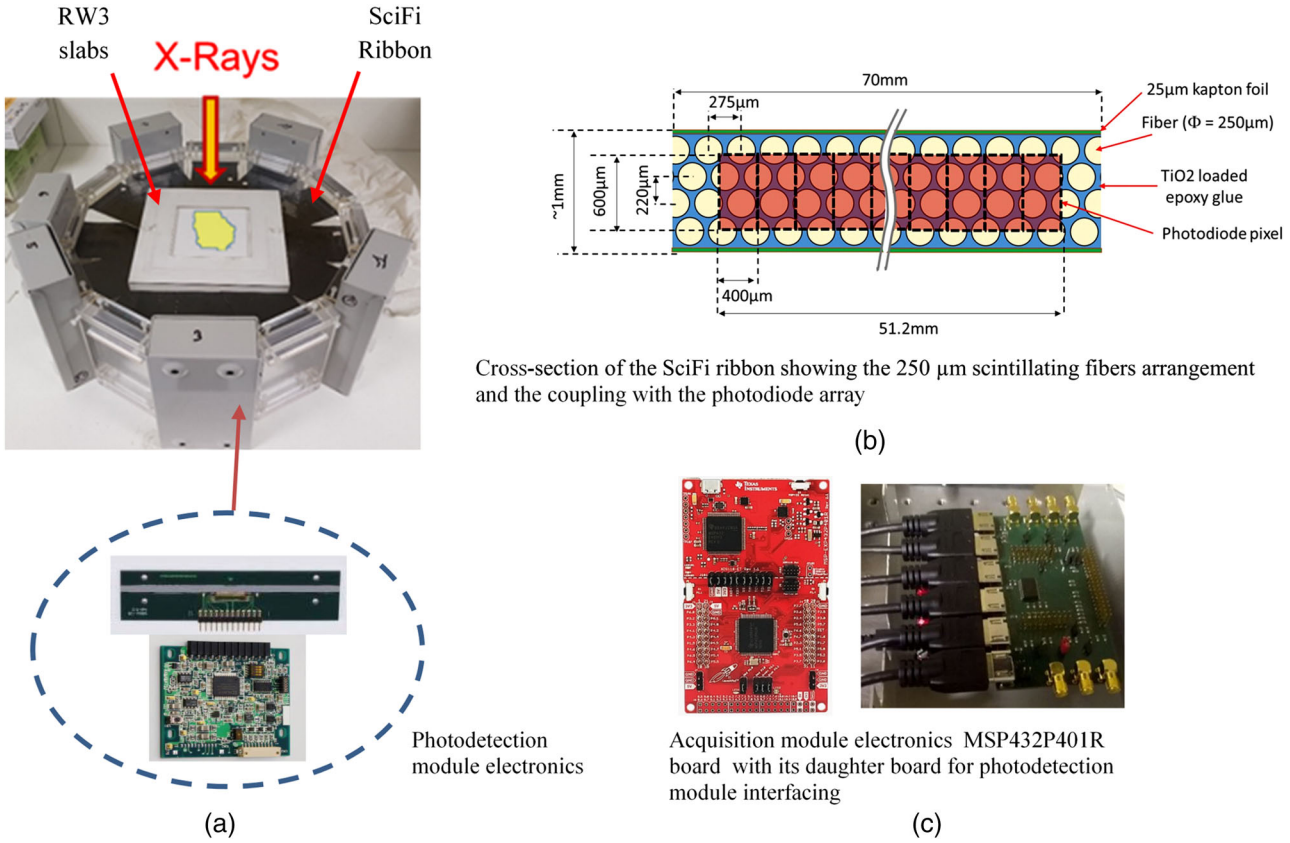

FIGURE 1 (a) Instrumented phantom prototype, (b) cross-section of the SciFi ribbons, and (c) signal acquisition electronics

We have compared testing results with EBT3 film measurements and performed two-dimensional (2D) gamma index analysis with 2%-dose-difference (DD)/700-μm-distance-to-agreement (DTA) and 1%-DD/1-mm-DTA criteria.

2 | MATERIALS AND METHODS

2.1 | Small-field QA phantom prototype

The small-field QA phantom is built using a 190 × 190 × 135-mm^3 RW3 material (Easy Slab, LAP GmbH, Germany) as a solid-water bloc, to ensure sufficient dose contribution from backscattered particles of the medium.

Six water-equivalent scintillating fiber ribbons are stacked with in-plane 30° rotated increments to form a field-size detector with a ribbon overlapped area of about 42 mm in diameter. The detector is placed at the depth of maximum dose (i.e., 1.4 cm from the RW3-irradiated surface for 6-MV beams[17]). Each scintillating ribbon is based on the SciFi detector technology initially developed for the LHCb experiment at CERN and recently proposed for small-field radiotherapy QA.[18–20] The ribbon integrates four layers of Kuraray SCSF-78-MJ scintillating fibers (as shown in Figure 1b), each consisting of a polystyrene core (n_{core} = 1.59) surrounded by two 10-μm-thin claddings (nc_{lad1} = 1.49, and n_{clad2} = 1.42). The fibers have an outside diameter of 250 μm. The tissue-equivalent response of the detector is given by the 1.05-g/cm^3 density of the polystyrene fiber core.[17] The four-layer ribbon has 40 cm in length, 70 mm in width, and ~1 mm in thickness, incorporating about 1000 fibers. The multilayered fiber integration in a ribbon has been optimized with 25% TiO_2-filled epoxy glue to minimize optical crosstalk between adjacent fibers.[21] The four-layered ribbon was decided according to optimal coupling to the array of photodiodes (see Figure 1) on the one hand, and better mechanical robustness (compared to single-layer ribbon) on the other.

Unlike fiber-coupled point detectors, where Cerenkov contribution (stem effect) due to irradiated readout fibers should be considered and minimized,[22,23] our fiber ribbon detector produces scintillating signal, including Cerenkov component. The scintillating signal at each ribbon output corresponds to projected irradiation field along the fibers axis. It is detected by a 128 silicon photodiode linear array with 400-μm-pixel pitch and implementing CMOS charge pre-amplification (S11865-128 and C9118, Hamamatsu Photonics K.K., Japan). The sensitivity of the photodiode pixel is 1500 V/lx s in chosen high gain conditions.

TABLE 1 Main characteristics

Number of tissue-equivalent scintillating ribbons	Six (rotated increment of 30°)
Number of scintillating fibers	~6000 (6 × 1000)
Lateral resolution (pixel pitch of the photodiode arrays)	400 μm
Number of photodetection channels	768 (6 × 128)
Maximum field size (corresponding to the area where the ribbons overlap)	42 mm in diameter
Detector depth in RW3	1.4 cm

Signals from the six ribbons are read out synchronously and acquired by a module based on an MSP432P401R board (Texas Instruments Inc, USA) that includes a 48-MHz 32-bit ARM Cortex M4F and 16-bit SAR ADC. The acquisition module is connected by a USB to a laptop for the data processing.

The small-field QA phantom prototype is shown in Figure 1, and its main characteristics are summarized in Table 1.

The light emitted by each scintillating fiber is proportional to the integral dose along the fiber length weighted by its optical attenuation and scintillation efficiency.[24] The signal at each ribbon output therefore represents a projected view of the irradiation field as illustrated in Figure 2a.

The outputs of the six stacked fiber ribbons implemented in the QA phantom prototype provide six projected views of the dose profiles depending on the angle between collimator's X-axis and the corresponding ribbon, $\theta_i|_{i=1\ldots6}$ as shown in Figure 2b. Each profile is acquired by the 400-μm-pitch linear array of photodiodes and then processed by linear interpolation to obtain 100-μm pixel size for matrix computations.

2.2 | Dose distribution reconstruction methods

We propose a two-step reconstruction method of the 2D dose distribution from the six measured projected profiles.

The first step is to apply the geometric tomography approach proposed by Desbat et al.[25] This moment-based method identifies irradiation field geometry parameters (e.g., the center, orientation, width, and length of the field) by assuming first no penumbra of the X-ray field, as illustrated in Figure 3a. These parameters are computed from the moments of order 0, 1, and 2 of the projections that yield the estimation of the corresponding moments of the field, that is, the mass, the center of mass, and the covariance matrix M, respectively. The authors also evaluated the robustness of this method by simulations, giving submillimeter uncertainties in the presence of 50% multiplicative Gaussian noise in the sinogram.[25]

The rectangular field parameters are determined by using the diagonalization of the covariance matrix M as follows:

$$M \begin{bmatrix} v_{A1} & v_{B1} \\ v_{A2} & v_{B2} \end{bmatrix} = \begin{bmatrix} v_{A1} & v_{B1} \\ v_{A2} & v_{B2} \end{bmatrix} \begin{bmatrix} \lambda_A & 0 \\ 0 & \lambda_B \end{bmatrix} \quad (1)$$

with $\begin{bmatrix} v_{A1} \\ v_{A2} \end{bmatrix}$ and $\begin{bmatrix} v_{B1} \\ v_{B2} \end{bmatrix}$ the eigen vectors of M and λ_A and λ_B the eigen values such that $\lambda_A \geq \lambda_B > 0$. As shown by Desbat et al.,[25] the orientation of the field corresponds to the angle between the vector $\begin{bmatrix} 1 \\ 0 \end{bmatrix}$ and the eigen vector $\begin{bmatrix} v_{A1} \\ v_{A2} \end{bmatrix}$. The length l and the width w of a rectangular field are estimated by $l = \sqrt{12\lambda_A}$ and $w = \sqrt{12\lambda_B}$. In the case of an elliptic field, they are given by $l = \sqrt{\lambda_A}$ and $w = \sqrt{\lambda_B}$.

The second step is to evaluate the dose distribution with penumbra consideration. This penumbra has been modeled using Gaussian convolution by Desbat et al.[25] However, this model is less accurate for small fields due to source occlusion with penumbra overlap. We have therefore adopted an alternative approach to model the penumbra, based on superimposition of several dose slices of decreasing size and centered on the field center, as illustrated in Figure 3b.[19] This approach is not based on the assumption of Gaussian penumbra shape and may allow better accuracy achievement for small fields with penumbra overlap.

In our previously published paper, the dose distribution reconstruction method could only be used for fields defined by stereotactic cones as it was using (i) only one projected profile and (ii) dose slices with disk shapes thanks to the symmetry of revolution of the field.[19] In the following, we extend this approach to small rectangular and elliptic fields where measurements of six projected profiles are used for 2D dose distribution determination.

The penumbra can then be modeled by a superimposition of dose slices of decreasing sizes as illustrated in Figure 4 for a 20 × 10 mm^2 rectangular field.

The dose shapes are derived from the field size (l, w) and orientation previously determined by geometric tomography.

About 50 dose slices are used to determine the penumbra with about 2% dose increment between consecutive slices. As illustrated in Figure 5, the length of the jth dose slice, l_j, is determined as follows: (i) choose among six projected profiles, the one having the widest dose distribution; (ii) l_1 corresponds to the full width of the chosen profile at 2% of its maximum, l_2 to the full width at 4% of its maximum and so on.

The width w_j of the jth dose slice as a function of its length l_j is computed as follows:

$$w_j = l_j - l + w \quad (2)$$

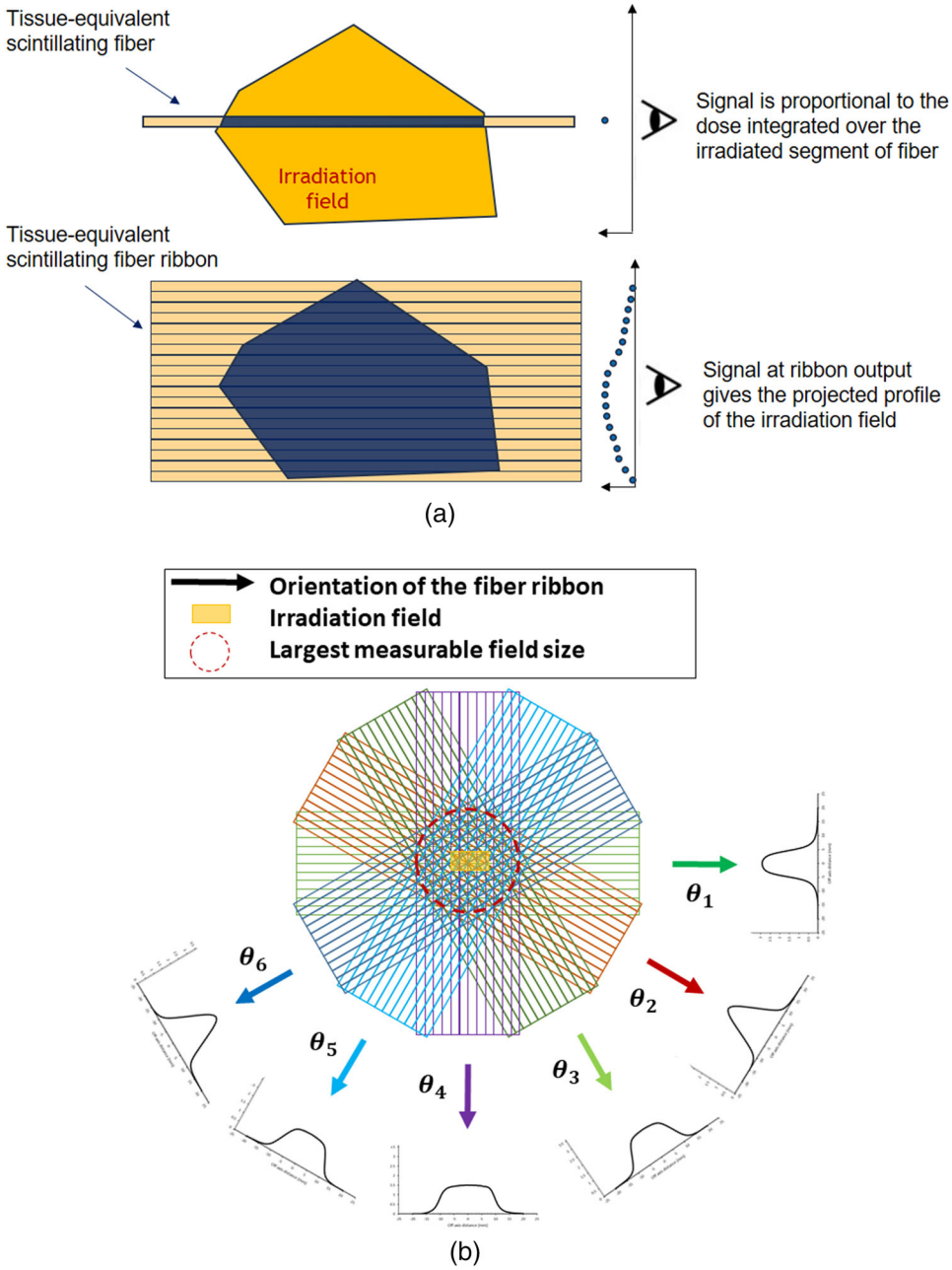

FIGURE 2 Scintillating signals at the outputs (a) of a single fiber and of a fiber ribbon, (b) and the quality assurance (QA) phantom

For the *j*th dose slice geometry, P_j, the projected profile along the *l*th ribbon axis is computed. It provides the corresponding relative response of the *k*th photodiode coupled to the ribbon. It can be written in vector form as follows:

$$P_j = \begin{bmatrix} p_{j,l1} \\ \vdots \\ p_{j,lk} \end{bmatrix} \tag{3}$$

The "thickness" of the *m* dose slices can be determined as the nonnegative least-squares solution of the linear system of equations expressed in matrix form:

$$\begin{bmatrix} S_{11} \\ \vdots \\ S_{1k} \\ \vdots \\ S_{61} \\ \vdots \\ S_{6k} \end{bmatrix} = \begin{bmatrix} p_{1,11} & \cdots & p_{m,11} \\ \vdots & & \vdots \\ p_{1,1k} & \ddots & p_{m,1k} \\ \vdots & & \vdots \\ p_{1,61} & & p_{m,61} \\ \vdots & & \vdots \\ p_{1,6k} & \cdots & p_{m,6k} \end{bmatrix} \begin{bmatrix} \beta_1 \\ \vdots \\ \\ \vdots \\ \\ \vdots \\ \beta_m \end{bmatrix} \tag{4}$$

where S_{mn} is the signal detected by the *n*th pixel of the photodiode array coupled to the *m*th ribbon, β_j is the

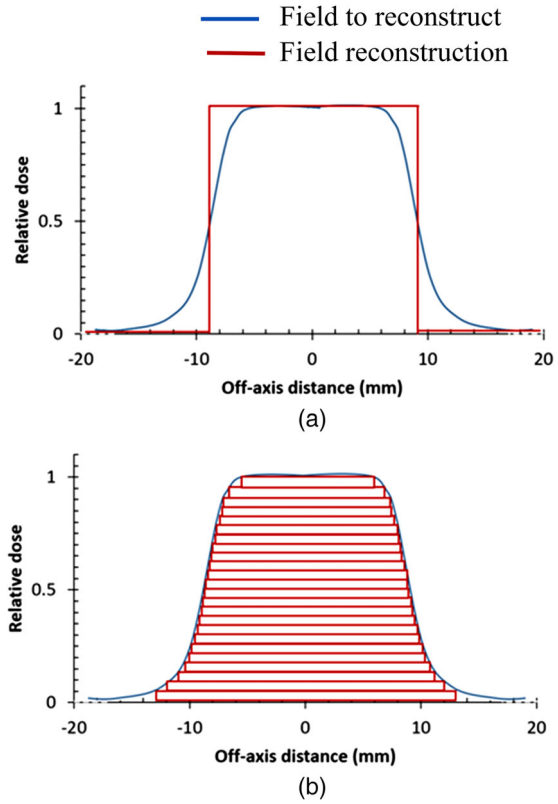

FIGURE 3 Principle of the two-step reconstruction methods illustrated in one dimension (1D): (a) geometric tomography assuming no penumbra of the X-ray field and (b) penumbra modeling superimposition of slices of decreasing size and centered on the field center

estimated thickness of the *j*th dose slice, as shown in Figure 4.

This solution can be calculated by using a nonnegative linear least-squares algorithm. We used *lsqnonneg* available in MATLAB.

The relative dose at any (x, y) position is given by

$$D_r(x,y) = \sum_{j=1}^{m} \delta_j(x,y)\,\beta_j \tag{5}$$

where $\begin{cases} \delta_j(x,y) = 1 \text{ if the } (x,y) \text{ position is within the } j \\ \text{th dose slice } \delta_j(x,y) = 0 \text{ otherwise} \end{cases}$

For the validation of the two-step reconstruction method, we used FBP and SIRT as reference methods for comparison as implemented in the Astra-toolbox in MATLAB.[16]

2.3 | Prototype testing conditions

All the measurements presented in this paper were carried out at the radiotherapy department of the University Hospital of Lyon (Centre Hospitalier Lyon Sud). Radiation was provided from Novalis TrueBeam STX (Varian Medical Systems Inc, USA) to deliver 6-MV flattened photon beam at a dose rate of 600 MU/min. Two rectangular fields of 20 × 10 and 10 × 10 mm^2 were set by an HD120 high definition MLC, whereas the circular and elliptic fields were obtained by using 5- and 10-mm stereotactic cones, respectively. The gantry angle of 30° shown in Figure 6 gave an aspect ratio of 1.15 for the elliptic field.

The phantom was placed at source detector distance (SDD) of 100 cm, with collimator angles of 0° and 45° for testing in best and worst cases, respectively. (The 0° angle is a favorable configuration for tomographic field reconstruction as two ribbons are aligned with the main field axis, whereas the 45° one corresponds to the most unfavorable configuration with maximum misalignment between main field axes and ribbons.) It was positioned to be aligned with the room lasers conventionally employed to project the LINAC axis and isocenter for patient positioning. This ensured that the radiation field is within the detector area (this positioning was not critical as the actual position of the detector is determined during the 2D field reconstruction) and that the first and fourth scintillating ribbon axes were aligned with LINAC axes.

For signal acquisition, the integration time of the charge preamplifiers was adjusted from 15 to 50 ms for each field size to fit the full 16-bit ADC dynamic range. Each projected profile was measured by averaging 40 acquisitions of the photodetected scintillating signal at the ribbon output, which corresponded to 6–20 MU at the LINAC output.

The calibration of the phantom was carried out in two steps.

The actual positions and angles of the ribbons were measured by using a 40-kV X-ray image of the phantom acquired with the on-board-imager X-ray tube of the LINAC. The measured angles were of 0.89°, 30.59°, 60.55°, 89.17°, 121.1°, 150.8°, very close to the design values from 0° to 150° with an increment of 30°. X-ray images can also be used to assess the quality of the phantom alignment on LINAC axes based on the room lasers, which was within ±1°.

For calibrating the 768 acquisition channels, the phantom was irradiated by using a 10 × 10-cm^2 field with additional RW3 slabs on the top surface in order to place the scintillating ribbons at an equivalent depth in water of ∼10 cm (where in-field dose distribution is flat thanks to the flattening filter). The validation of the calibration coefficients was finally operated by irradiations with a 3 × 3-cm^2 field and collimator angles set to the measured ribbon angles.

It is worth mentioning that this 3 × 3-cm^2 calibration field fulfills the requirements from IAEA–AAPM TRS-483 for machine-specific reference fields.[2]

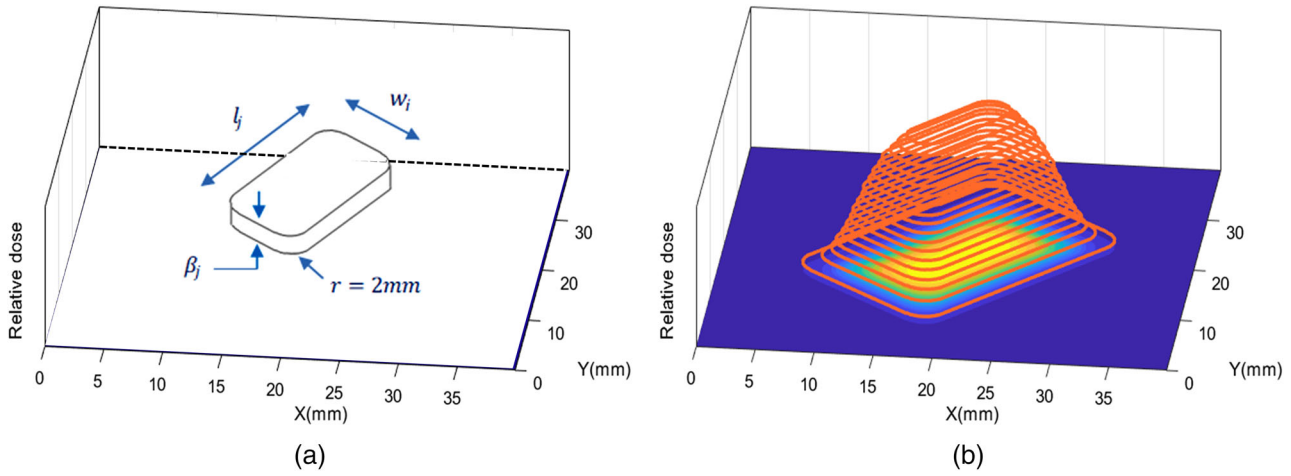

FIGURE 4 Second step of the dose distribution reconstruction method: (a) dose slice definition with its thickness β_j that represents the dose increment and l_j, w_j its length, and width, respectively, and (b) penumbra modeling by a superimposition of dose slices for a 20 × 10-mm^2 6-MV rectangular field

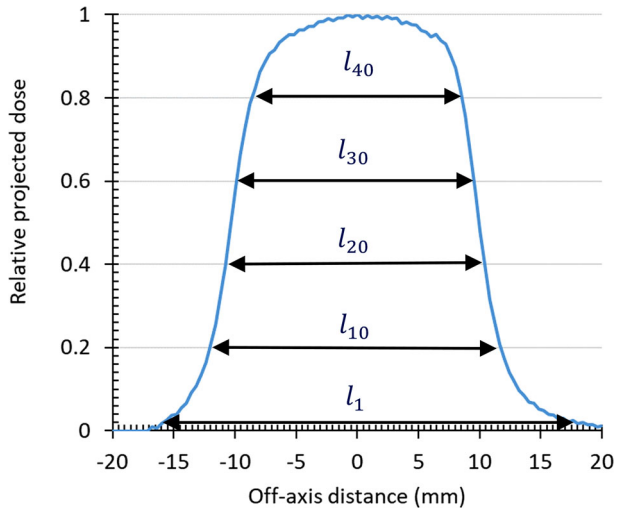

FIGURE 5 Second step of the dose distribution reconstruction method: automatic determination of dose slices lengths, l_j, from the measured projected profile along the small side for a 20 × 10-mm^2 6-MV rectangular field

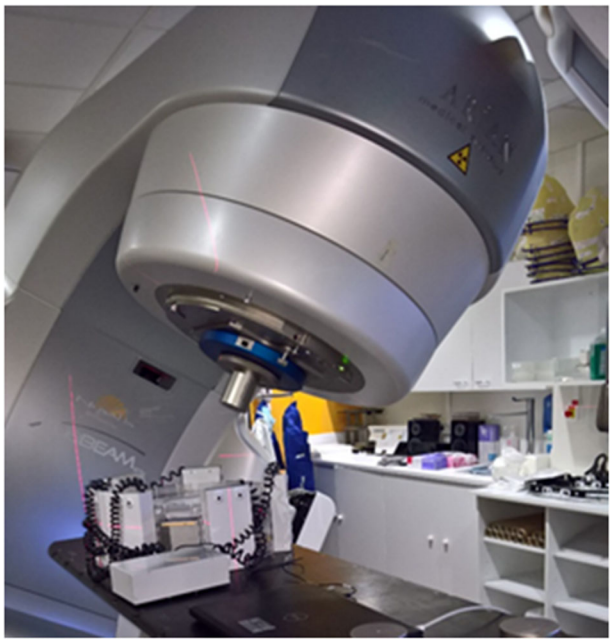

FIGURE 6 Irradiation setup for irradiation with an elliptic field: The LINAC is equipped with a 10-mm stereotactic cone and a 30° gantry is used.

2.4 | Reference data

For each tested field, the reference dose distributions were measured by using EBT3 Gafchromic films irradiated in the same conditions, that is, 6-MV flattened photon beam, SDD = 100 cm and skin–source-distance = 98.6 cm with a dose of 100 MU.

The EBT3 films were scanned with a resolution of 300 pixels per inch, and the dose distribution was determined by using the green color channel of images. The film response to the dose was linearized according to the method of Devic et al. based on the net optical density.[26]

3 | RESULTS

3.1 | Signal at the phantom outputs

Figure 7a,b shows the six measured profiles for the 20 × 10-mm^2 rectangular and elliptic fields, respectively. The collimator angle was set at 0° for these measurements.

Note that the six directions are acquired synchronously on the same beam fluence within less than 2 s. The lateral resolution of the measured profiles is

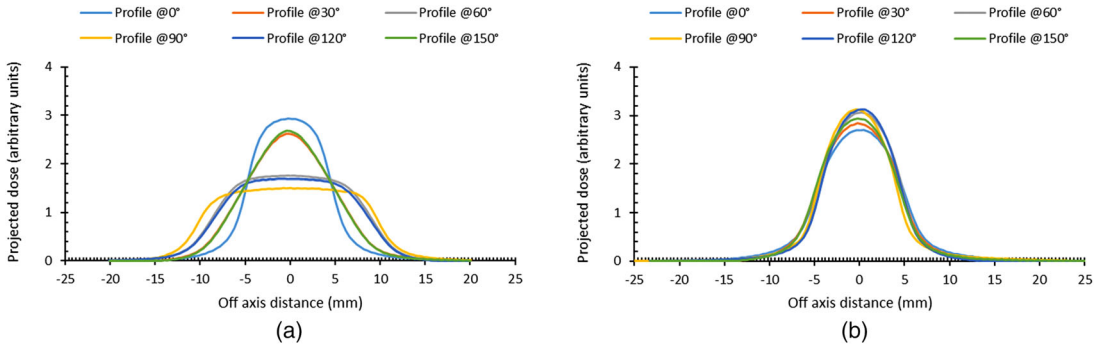

FIGURE 7 Measured profiles for (a) the 20 × 10-mm^2 rectangular and (b) the elliptic fields

limited by the pixel pitch of the photodiode arrays that is 400 μm.

Figure 7a shows the six profiles at the ribbons' outputs. The profiles have different shapes and maximum levels depending on the angle between the collimator's *X*-axis and ribbon, θ_i, as illustrated in Figure 2b. The 30° and 150° curves are almost the same due to the symmetry of a rectangular field. This is also the case for 60° and 120° curves. These six measured profiles are used to determine the left term of Equation (4), allowing calculations of 2D dose distribution. These profiles were acquired with an estimated signal-to-noise ratio (SNR) of ∼50 dB for 15-ms integration time (the SNR was evaluated for the in-the-field portion of the profile and calculated as the mean value for 40 independent signal acquisitions divided by the standard deviation). Each projected profile in Figure 7a was measured by the averaged values over these 40 acquisitions with an SNR of ∼66 dB. Despite an aspect ratio as low as 1.15 for the elliptical field, the small variations in height and width between the different curves in Figure 7b are still observable. The SNR was evaluated to be of ∼28 and ∼44 dB for 15-ms integration time and after averaging, respectively, and allows the reconstruction of elliptic dose distribution.

3.2 | Dose distribution model based on dose slices superimposition

As explained in Section 2.2, we propose a dose distribution model based on the superimposition of *m* dose slices of decreasing sizes and centered on the beam axis.

The number of dose slices as well as their sizes can automatically be determined according to the gradients of the measured projected profiles.

Figure 8 shows three projected profiles obtained from model computations (i.e., the right side of Equation 4 with $m = 46$), and from measurements. We observe a good fit between the modeled and measured data with relative differences lower than 9%.

Figure 9a shows the reconstructed dose distribution with 46 dose slices for the 20 × 10-mm^2 field. The *X* and *Y* dose profiles are exhibited in Figure 9b,c, respectively.

It can be seen from this figure that differences in sizes between adjacent slices are related to the dose gradient in the field edge: the smaller the difference, the higher the gradient.

Figure 10 compares dose profile of the 20 × 10-mm^2 field between reconstruction and EBT3-film measurements: *X*-axis dose profile (Figure 10a) and *Y*-axis one (Figure 10b).

The beam profile parameters (FWHM and 20%–80% penumbra width) extracted from the profiles of Figure 10 are presented in Table 2. The differences of these parameters between reconstruction and film measurements remain submillimeter.

3.3 | Gamma index analysis for the two-step reconstruction method

The performance of the two-step reconstruction method has been evaluated by 2D global gamma analysis with 2%-DD/700-μm-DTA or 1%-DD/1 mm-DTA criteria and 10% threshold, with reference dose map determined by EBT3 film measurements. The used criteria are more tight than the 2%-DD/2 mm-DTA ones, which is routinely used at the hospital.

For comparison, 2D global gamma analysis has also been carried out on dose distributions reconstructed by FBP and SIRT methods.

Dose distributions obtained with the three reconstruction methods as well as the gamma index map are presented in Figure 11 for the 20 × 10-mm^2 field with a collimator angle of 45°. All the three methods give consistent dose distributions with better results for the two-steps and FBP reconstructions methods. Because of the 10% threshold applied to the film reference, the reconstruction artifacts visible on FBP and SIRT images for the off-field positions are not taken into account in the gamma analysis.

Tables 3 and 4 compare the gamma index pass rates between reconstruction methods for seven field

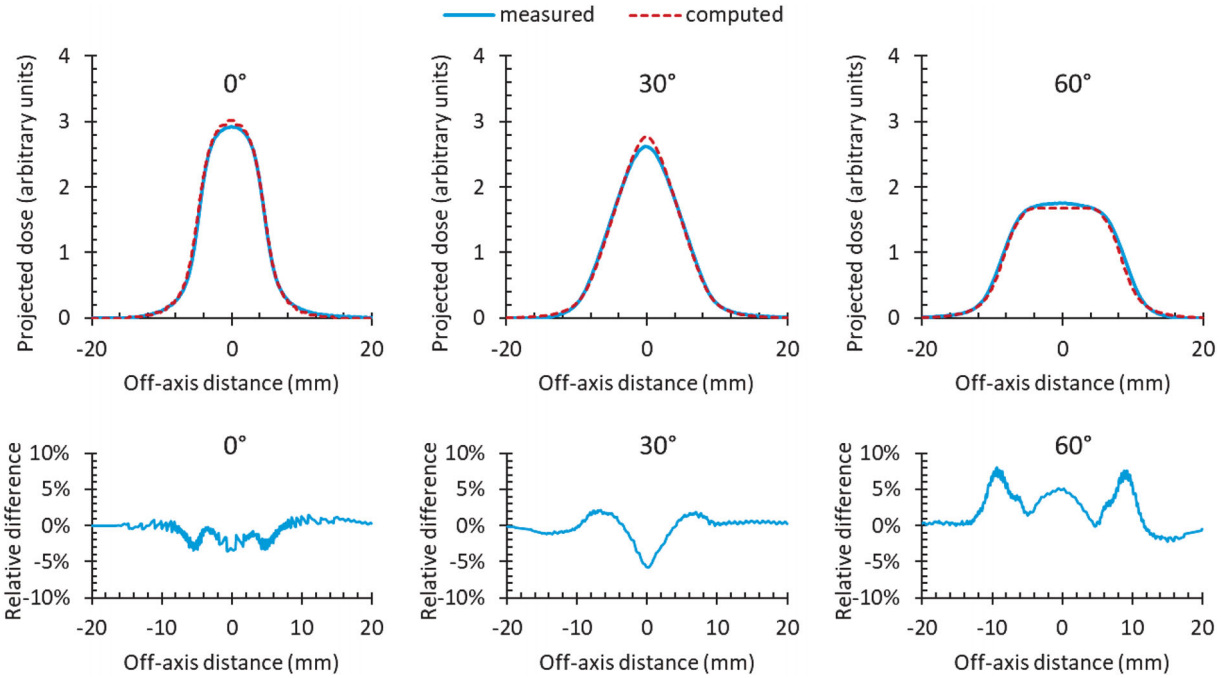

FIGURE 8 Comparison between computations and measurements on projected profiles at three different angles, using 20 × 10-mm^2 field, 0° collimator angle, and 46 dose slices. The differences between measurements and computations are plotted relatively to the maximum of the computed profile.

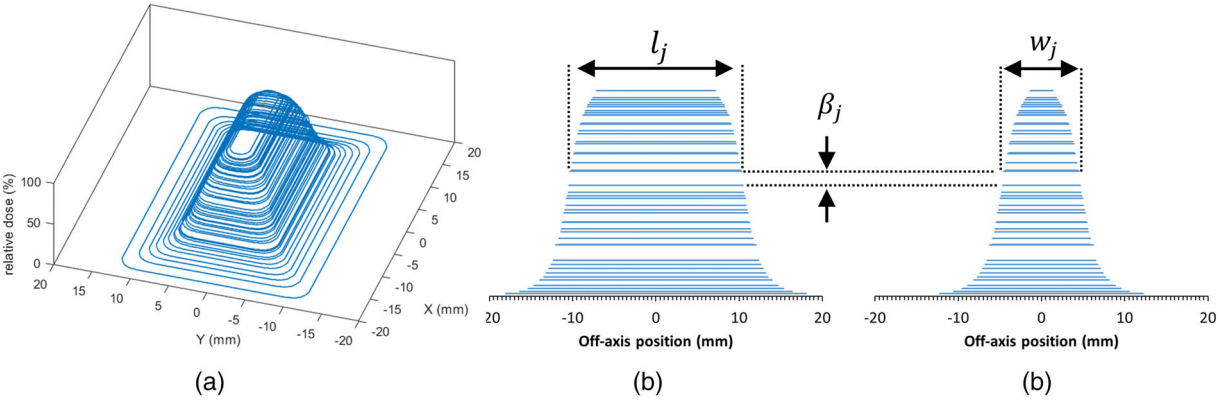

FIGURE 9 (a) Dose distribution for the 20 × 10-mm^2 field, reconstructed with 46 dose slices and (b) *X* and (c) *Y* dose profiles. The blue lines show the slices.

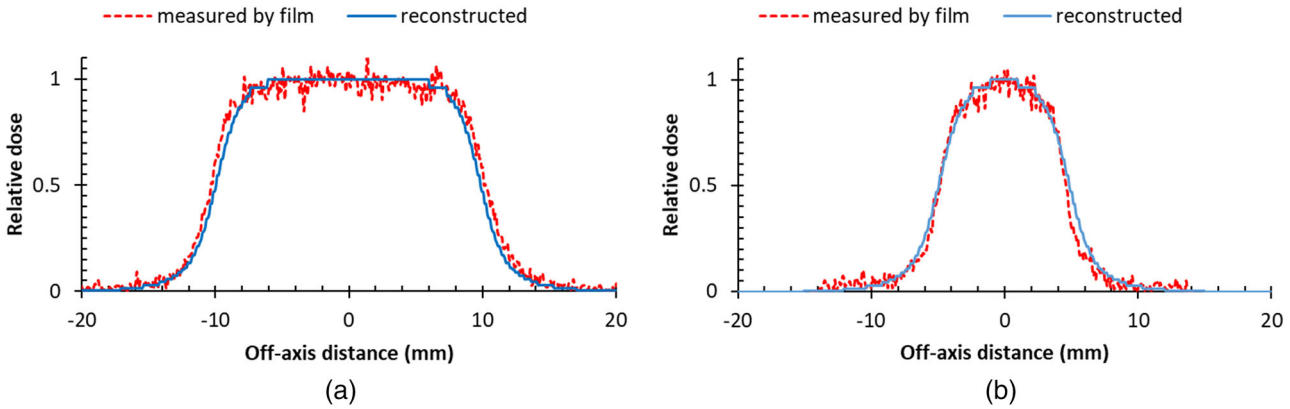

FIGURE 10 Dose profile of the 20 × 10-mm^2 field obtained by two-step method reconstruction and EBT3-film measurements: (a) *X*-axis dose profile and (b) *Y*-axis one

TABLE 2 Beam profile parameters of the 20 × 10-mm^2 field determined on the profiles of Figure 10

Field parameters	FWHM		20%–80% penumbra width[a]	
	X profile (mm)	*Y* profile (mm)	*X* profile (mm)	*Y* profile (mm)
Reconstructed profiles	19.7	9.7	2.8	2.8
EBT3 measurements	20.5	9.4	2.6	1.9

[a]The 20%–80% penumbra width is calculated as the average between the 20% and 80% rising and falling parts on the beam profiles.

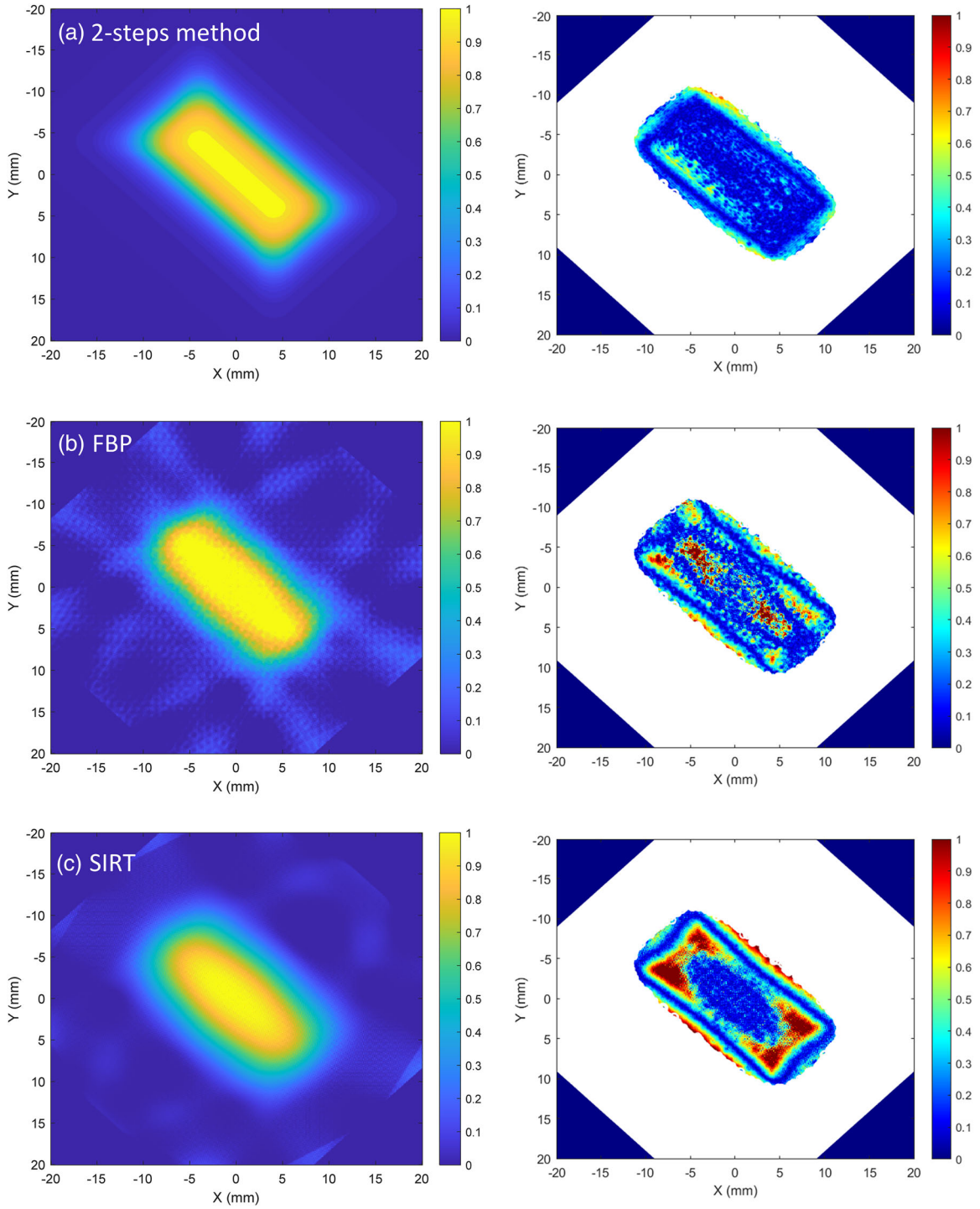

FIGURE 11 Dose distributions and 1% dose-difference (DD)/1 mm distance-to-agreement (DTA) gamma index maps obtained with the (a) two-step, (b) filtered back projection (FBP), and (c) simultaneous iterative reconstruction technique (SIRT) reconstruction methods for the 20 × 10-mm^2 field

TABLE 3 Gamma index analysis with a low-dose threshold of 10%, a dose-difference of 2% and a distance to agreement of 700 μm, for the tested fields

Field	Collimator orientation (°)	Two-step method	FBP	SIRT
20 × 10 mm^2	0	99.9	98.7	94.2
	45	99.4	98.0	88.6
10 × 10 mm^2	0	98.4	99.1	89.9
	45	96.9	99.6	90.4
Elliptical field (cone 10 mm—gantry 30°)	0	99.9	94.1	65.3
	45	99.9	97.5	66.6
Cone 5 mm	0	98.9	87.9	51.7

Abbreviations: FBP, filtered back projection; SIRT, simultaneous iterative reconstruction technique.

TABLE 4 Gamma index analysis with a low-dose threshold of 10%, a dose-difference of 1% and a distance–to-agreement of 1 mm, for the tested fields

Field	Collimator orientation (°)	Two-step method	FBP	SIRT
20 × 10 mm^2	0	99.9	98.2	95.9
	45	99.8	97.5	92.5
10 × 10 mm^2	0	99.9	99.4	97.0
	45	99.6	99.8	97.4
Elliptical field (cone 10 mm—gantry 30°)	0	99.9	96.9	84.9
	45	99.9	99.0	86.5
Cone 5 mm	0	99.8	93.4	65.6

Abbreviations: FBP, filtered back projection; SIRT, simultaneous iterative reconstruction technique.

configurations. The two-step and FBP methods systematically outperform SIRT that is adversely affected by the small number of projected views. Moreover, higher gamma index pass rates are obtained with the two-step method than with FBP in the case of the fields defined with the stereotactic cones, because FBP reconstruction of circular and elliptic fields is penalized by the small number of projected views (i.e., 6) acquired by the prototype.

For all the tested configurations, reconstructed data with the two-step method systematically pass the gamma index criteria with success rates higher than 95%, which confirms the submillimeter accuracy achieved by the proposed phantom (accuracy required for small-field QA). It also indicates that the gamma pass rate of this two-step reconstruction method could be degraded in the case of a very small rectangular field.

4 | DISCUSSION

4.1 | System manufacturing

As shown in Table 1, the proposed system implements a very large number of scintillating fibers (6 ribbons of ∼1000 fibers, each measuring 40-cm long). Despite this apparent complexity, it is based on the mature SciFi technology developed and optimized for the CERN LHCb project (more than 1300 ribbons of ∼2800 fibers have been produced in this framework, each measuring 2.5-m long). It also benefits from the associated mass production facilities (available in Lausanne, Dortmund, Aachen and Kurchatov) for reliable and cost-effective ribbon manufacturing.[18]

4.2 | Phantom performances

The QA phantom with six scintillating ribbons for detecting dose distributions has been tested successfully. Each scintillation ribbon is coupled to the photodiode linear array and provides a lateral resolution of 400 μm. Scintillation signal from each fiber is proportional to the integral dose received along the fiber direction. This detector configuration allows the verification of the 2D dose distribution in small rectangular and elliptic fields. The gamma index analysis with 2%-DD and 700-μm-DTA criteria gives a pass rate for these reconstructed 2D distributions over 95%. These results are obtained with the scintillating ribbons that are water equivalent (based on the polystyrene scintillating fiber core), thus corresponding to the recommendations from the TRS-483 international Code of Practice for the relative dosimetry of small photon fields.[27]

In a previously published study,[19] we have also shown that such a scintillating-ribbon-based phantom can be used for the real time verification of the output factor for fields defined by stereotactic cones with sizes down to 4 mm. It allowed real-time determination of field output factor, with measured errors for all cone sizes within ±1.6% in comparison with data from IRSN measured by combining EBT3 films and TLD dosimeters. Like other plastic detecting systems,[6,24,25] our proposed detector has the advantage of being water equivalent with lower energy dependence and dose perturbations, in comparison with inorganic scintillating detectors.[13,14,28]

These results on the phantom prototype confirm the feasibility of developing systems based on water-equivalent scintillating ribbons for small-field QA. They are in-line with the state of the arts and compare well with the performances achieved by QA systems based on a high spatial resolution diode array.[27,29] A recent paper presented the use of an array of 1013 *n*-type solid state diodes for small-field QA.[30] The diodes, with a 0.48 × 0.48-mm^2 active area, were distributed with a diagonal center-to-center separation of 2.47 mm. The authors found that in 95% of the cases, the gamma results were above 90% when compared to film measurements (with 3% DD and 1-mm DTA criteria). However, the reported results were obtained on mean effective field sizes ranging from 4.9 to 60 mm and no detailed information was provided on the performances obtained for the smallest field sizes. Our results give comparable gamma pass rates but with more tight 2%-DD/700-μm-DTA and 1%-DD/1 mm-DTA criteria. It can be explained by the 400-μm lateral resolution of the phantom prototype in comparison with the 2.47-mm diagonal center-to-center separation in the diodes array.

Another study reported the use of a 2D solid-state dosimeter with 505 diodes spaced by 0.2 mm for small-field QA and more specifically for output factor and effective field size measurements.[27] This system determines *X* and *Y* profiles with an accuracy lower than 100-μm-DTA for any dose level as compared to EBT3 film measured profiles. However, it has only two perpendicular linear arrays of diodes and could not be used for 2D dose QA of small-fields.

Compared to recently proposed point detectors for small-field dosimetry,[13,14,31] our system operates with no mechanical displacement and in synchronized parallel signal acquisition, which is favorable in terms of repeatability and time required to measure a complete 2D dose distribution with submillimeter resolution.

4.3 | Dose distribution reconstruction method

The proposed two-step reconstruction method, which combines geometric tomography and a penumbra estimation by superimposition of dose slices, has been validated on experimental data. It allows efficient and accurate dose reconstruction as confirmed by evaluated 2D gamma index pass rates with submillimeter criteria. This method uses an a priori knowledge of the field shape, for example, rectangular or elliptic, which is determined by the type of collimator used to define the field (i.e., the MLC for the rectangular fields and the stereotactic cones for the elliptic ones). This knowledge is used in geometric tomography step to compute the field size (using $l = \sqrt{12\lambda_A}$ and $w = \sqrt{12\lambda_B}$ for the rectangular fields and $l = \sqrt{\lambda_A}$ and $w = \sqrt{\lambda_B}$ for the elliptic fields, as explained in Section 2.2). It also defines the shape of the model for the dose slices used in the second step of the reconstruction algorithm. It is possible to implement the proposed reconstruction algorithm without this a priori knowledge: The algorithm is implemented for both types of fields and the field geometry corresponds to the one with the lowest residual when solving Equation (4).

Small square fields actually produce radiation areas with rounded corners with almost elliptical shapes, which deviate from the shape of Figure 4a. It can explain the degradation of the gamma passing rate of the two-step reconstruction method in the case of very tight DTA (Table 3). Méndez et al. have recently shown that the geometry of small square fields can be accurately described by superellipses, a family of curves encompassing shapes between ellipses and rectangles.[32] We will investigate the use of superellipses as dose slice shapes for the two-step small square field reconstruction method.

It is worth mentioning that the number of dose slices and their sizes (w_j, l_j) are determined automatically from the measured projected profiles. The number of doses slices (~50) is chosen according to the 2% DD criterion for the gamma index analysis. With this number of slices and the slice selection based on the projected profiles, the linear system of Equation (4) remains well conditioned. However, as observed in Figure 9, the dose increments from one slice to the next one, β_j, can vary significantly in the stack. It is possible to obtain smoother penumbra estimation by adding the following step: determine a refined set of $(w\prime_j, l\prime_j)$ by a regular "slicing" of *X* and *Y* reconstructed dose profiles and use it to update the least-squares solution of Equation (4). We observed larger differences between the penumbra values determined on the reconstructed and EBT3-measured profiles of the 20 × 10-mm^2 field compared to the differences published in our previous paper for the fields defined by the stereotactic cones.[19] This is due to the fact that the reconstruction algorithm assumes that the shape of the penumbra is identical in *X* and *Y*, which is true for the circular fields defined by the cones but not for the rectangular fields defined by the MLC (as confirmed by the film measurements). However, these differences remain in all cases submillimeter, which is acceptable. It is also noted that the proposed 2D

dose reconstruction method can be extended to more complex shapes defined by the MLC[33] (by using the a priori knowledge of the leaves geometry).

It is also possible to improve the quality of 2D dose reconstruction by using more scintillating ribbons, without increasing significantly the system complexity.[24] For such a case, thinner scintillating ribbons should be developed for the stack, using SciFi technology or planar scintillating waveguide.

Goulet et al. proposed a tomographic reconstruction of 2D dose distributions acquired by rotating a few scintillating fibers aligned in parallel. They obtained a millimeter resolution dose acquisition on a complete 2D plane. Our work represents a further step in the concept of tomodosimetry, meeting the QA requirements of small-fields and achieving submillimeter resolution.

Maximum-likelihood expectation-maximization-iterative reconstruction algorithm employed by Goulet et al. was also used more recently by Rilling et al. for establishing the proof of concept of 3D dose tomography using plenoptic imagers and a plastic scintillator volume.[34] They obtained very encouraging results that open new perspectives for 3D dosimetric tomography. However, the 2D gamma pass rates with a 2%-DD/2 mm-DTA criterion reported in this study are less than 80% and are not compatible with small-field QA.

Our approach is less versatile than the Rilling's one but gives much better results on small circular and rectangular fields. Our system can be used for stereotactic cone radiosurgery QA as well as for machine QA. We are currently working on extending the proposed two-step method for IMRT segment reconstruction to use our system for patient-specific QA.

5 | CONCLUSION

For small-field QA, we propose a new phantom with an implementation of six highly spatially resolved scintillating fiber ribbons that are coupled with linear arrays of photodiodes for signal readout. We have also developed a novel 2D dose reconstruction method to process projected dose profiles measured by the six scintillating fibers ribbons. The system has been tested in clinical conditions for small fields defined by the MLC (20×10 and 10×10 mm^2) and by 5- and 10-mm stereotactic cones.

The measured 2D dose distributions show gamma index pass rates higher than 95% for all the tested configurations of field sizes and shapes as compared with EBT3 film measurements with both 2%-DD/700-μm-DTA and 1%-DD/1 mm-DTA criteria. It confirms the ability to reconstruct 2D dose distributions, even in steep dose gradient regions, with high accuracy and resolution.

The proposed QA system can also be used to determine field output factors for small fields, as shown in our previously published study.[19]

As the proposed phantom employs water-equivalent scintillating detectors, it is in-line with the recommendations of IAEA-AAPM TRS-483 code of practice without the need to implement correction factor.

ACKNOWLEDGMENT

With financial support from ITMO Cancer AVIESAN (Alliance Nationale pour les Sciences de la Vie et de la Santé, National Alliance for Life Sciences & Health—Grant no. 18CP125-00) within the framework of the Cancer Plan. This research is also supported by the LABEX PRIMES (ANR-11-LABX-0063) of Université de Lyon, within the program "Investissements d'Avenir" (ANR-11-IDEX-0007) operated by the ANR. SciFi fiber ribbons used in this study developed and produced with support from the Swiss National Science Foundation under contract 166208. INL coauthors acknowledge the support by DOSILAB AG and by Jérôme Degouttes.

CONFLICT OF INTEREST

The authors have no relevant conflicts of interest to disclose.

REFERENCES

1. Das IJ, Morales J, Francescon P. Small field dosimetry: what have we learnt?. *AIP Conf Proc*. 2016;1747:060001. https://doi.org/10.1063/1.4954111
2. Palmans H, Andreo P, Huq MS, Seuntjens J, Christaki KE, Meghzifene A. Dosimetry of small static fields used in external photon beam radiotherapy: summary of TRS-483, the IAEA–AAPM international code of practice for reference and relative dose determination. *Med Phys*. 2018;45(11):e1123-e1145. https://doi.org/10.1002/mp.13208
3. Andreo P. The physics of small megavoltage photon beam dosimetry. *Radiother Oncol*. 2018;126(2):205-213. https://doi.org/10.1016/J.RADONC.2017.11.001
4. Podgorsak EB. *Radiation Oncology Physics: A Handbook for Teachers and Students*. International Atomic Energy Agency; 2005.
5. Xicohténcatl-Hernández N, Moreno-Ramirez A, Massillon-JL G. Electron and photon energy spectra outside of 6 MV X-ray small radiotherapy field edges produced by a Varian iX Linac. *Front Phys*. 2021;9(September):1-10. https://doi.org/10.3389/fphy.2021.656922
6. Lam SE, Bradley DA, Khandaker MU. Small-field radiotherapy photon beam output evaluation: detectors reviewed. *Radiat Phys Chem*. 2021;178:108950. https://doi.org/10.1016/j.radphyschem.2020.108950
7. Aspradakis MM, Byrne JP, Palmans H, et al. IPEM report number 103: small field MV photon dosimetry. International Symposium on Standards, Applications and Quality Assurance in Medical Radiation Dosimetry (IDOS). Vienna, Austria; 9–12 November 2010.
8. Lopez AG, Antonio J, Sanchez V, Domingo J, Martin L. Small fields measurements with radiochromic films. *J Med Phys*. 2015;40(2):61-67. https://doi.org/10.4103/0971-6203.158667
9. Casar B, Gershkevitsh E, Mendez I, Jurković S, Huq MS. A novel method for the determination of field output factors and output correction factors for small static fields for six diodes and a microdiamond detector in megavoltage photon beams. *Med Phys*. 2019;46(2):944-963. https://doi.org/10.1002/MP.13318
10. Czarnecki D, Zink K. Monte Carlo calculated correction factors for diodes and ion chambers in small photon fields. *Phys*

Med Biol. 2013;58(8):2431-2444. https://doi.org/10.1088/0031-9155/58/8/2431
11. Benmakhlouf H, Sempau J, Andreo P. Output correction factors for nine small field detectors in 6 MV radiation therapy photon beams: a PENELOPE Monte Carlo study. *Med Phys*. 2014;41(4):1-12. https://doi.org/10.1118/1.4868695
12. Garnier N, Amblard R, Villeneuve R, et al. Detectors assessment for stereotactic radiosurgery with cones. *J Appl Clin Med Phys*. 2018;19:88-98. https://doi.org/10.1002/acm2.12449. April.
13. Debnath SBC, Fauquet C, Tallet A, et al. High spatial resolution inorganic scintillator detector for high-energy X-ray beam at small field irradiation. *Med Phys*. 2020;47(3):1364-1371. https://doi.org/10.1002/mp.14002
14. Alharbi M, Martyn M, O'Keeffe S, Therriault-Proulx F, Beaulieu L, Foley M. Benchmarking a novel inorganic scintillation detector for applications in radiation therapy. *Phys Med*. 2019;68(October):124-131. https://doi.org/10.1016/j.ejmp.2019.11.018
15. Olaciregui-ruiz I, Beddar S, Greer P, et al. In vivo dosimetry in external beam photon radiotherapy : requirements and future directions for research, development, and clinical practice. *Phys Imaging Radiat Oncol*. 2020;15(August):108-116. https://doi.org/10.1016/j.phro.2020.08.003
16. van Aarle W, Palenstijn WJ, Cant J, et al. Fast and flexible X-ray tomography using the ASTRA toolbox. *Opt Express*. 2016;24(22):25129. https://doi.org/10.1364/oe.24.025129
17. Beaulieu L, Goulet M, Archambault L, Beddar S. Current status of scintillation dosimetry for megavoltage beams. *J Phys Conf Ser*. 2013;444(1):2013. https://doi.org/10.1088/1742-6596/444/1/012013
18. Nieswand S. Production and quality assurance of a scintillating fibre detector for the LHCb experiment. *J Instrum*. 2017;12(02):C02071.1-C02071.12. https://doi.org/10.1088/1748-0221/12/02/C02071
19. Pittet P, Esteves J, Galvan JM, et al. SciFi detector and associated method for real-time determination of profile and output factor for small fields in stereotactic radiotherapy. *Med Phys*. 2020;47(4):1930-1939. https://doi.org/10.1002/mp.14019
20. Hopchev P. SciFi – a large scintillating fibre tracker for LHCb. The Fifth Annual Conference on Large Hadron Collider Physics. Shanghai, China. Shanghai Jiao Tong University; May 2017.
21. Kirn T. Nuclear instruments and methods in physics research a SciFi – a large scintillating fi bre tracker for LHCb Thomas Kirn, on behalf of the LHCb collaboration. *Nucl Inst Methods Phys Res A*. 2017;845:481-485. https://doi.org/10.1016/j.nima.2016.06.057
22. Liu PZY, Suchowerska N, Lambert J, Abolfathi P, McKenzie DR. Plastic scintillation dosimetry: comparison of three solutions for the Cerenkov challenge. *Phys Med Biol*. 2011;56(18):5805-5821. https://doi.org/10.1088/0031-9155/56/18/003
23. Beaulieu L, Beddar S. Review of plastic and liquid scintillation dosimetry for photon, electron, and proton therapy. *Phys Med Biol*. 2016;61(20):R305-R343. https://doi.org/10.1088/0031-9155/61/20/R305
24. Goulet M, Archambault L, Beaulieu L, Gingras L. High resolution 2D dose measurement device based on a few long scintillating fibers and tomographic reconstruction. *Med Phys*. 2012;39(8):4840-4849. https://doi.org/10.1118/1.4736526
25. Desbat L, Rit S, Clackdoyle R, Jalade P, Ribouton J, Pittet P. Geometric tomography for measuring rectangular radiotherapy fields from six projections. 2019 IEEE Nuclear Science Symposium and Medical Imaging Conference, NSS/MIC 2019. Institute of Electrical and Electronics Engineers Inc.; 2019. https://doi.org/10.1109/NSS/MIC42101.2019.9059657
26. Devic S, Tomic N, Deblois F, Seuntjens J. Linearization of dose – response curve of the radiochromic film dosimetry system. *Med Phys*. 2012;39(8):4850-4857.
27. Muñoz L, Kron T, Petasecca M, et al. Consistency of small-field dosimetry, on and off axis, in beam-matched linacs used for stereotactic radiosurgery. *J Appl Clin Med Phys*. 2021;22(2):185-193. https://doi.org/10.1002/ACM2.13160
28. Byrne K, Conlan S, Bazalova-Carter M, Foley M. Optimizing novel inorganic scintillation detectors for applications in medical physics. 2020 IEEE Sensors. IEEE; 2020:1-4. https://doi.org/10.1109/SENSORS47125.2020.9278758
29. Rose MS, Tirpak L, Van Casteren K, et al. Multi-institution validation of a new high spatial resolution diode array for SRS and SBRT plan pretreatment quality assurance. *Med Phys*. 2020;47(7):3153-3164. https://doi.org/10.1002/MP.14153
30. Rose MS, Tirpak L, Casteren KV, et al. Multi-institution validation of a new high spatial resolution diode array for SRS and SBRT plan pretreatment quality assurance. *Med Phys*. 2020;9:3153-3164. https://doi.org/10.1002/mp.14153
31. Galavis PE, Hu L, Holmes S, Das IJ. Characterization of the plastic scintillation detector Exradin W2 for small field dosimetry. *Med Phys*. 2019;46(5):2468-2476. https://doi.org/10.1002/mp.13501
32. Méndez I, Casar B. A novel approach for the definition of small-field sizes using the concept of superellipse. *Radiat Phys Chem*. 2021;189:109775. https://doi.org/10.1016/j.radphyschem.2021.109775
33. Pivot O, Clackdoyle R, Rit S, Desbat L. Estimation of radiotherapy dose fields from a few projections: how many projections will ensure uniqueness?. 2020 IEEE Nuclear Science Symposium and Medical Imaging Conference (NSS/MIC). Institute of Electrical and Electronics Engineers (IEEE); 2021:1-4. https://doi.org/10.1109/nss/mic42677.2020.9507859
34. Rilling M, Allain G, Thibault S, Archambault L. Tomographic-based 3D scintillation dosimetry using a three-view plenoptic imaging system. *Med Phys*. 2020;47(8):3636-3646. https://doi.org/10.1002/mp.14213

How to cite this article: Esteves J, Pivot O, Ribouton J, et al. A novel QA phantom based on scintillating fiber ribbons with implementation of 2D dose tomography for small-field radiotherapy. *Med Phys*. 2023;50:619–632. https://doi.org/10.1002/mp.15902